

Damage Assessment in FRP Through Digital Imaging and Computed Tomography

by

Mohammad Abdelghani, University of Alberta
Kari Arnston, University of Alberta
Renke Scheuer, Leibniz Universität Hannover
YuChin Wu, University of Alberta
Martin Doschak, University of Alberta
Pierre Mertiny, University of Alberta

Abstract

Damage assessment in Fiber Reinforced Plastics is a challenging task due to material inhomogeneity and anisotropy and manufacturing irregularities. Digital Image Correlation is a powerful tool for mapping surface deformations and strains. This allows for the observation of damage features such as interlaminar and intralaminar matrix cracking. However, DIC is limited in providing information on the cause of damage, which often initiates within the material. Computed tomography has the potential to overcome these challenges by providing highly localized information on material properties in FRP components. The present study explores the correlation between strain mappings, leakage initiation sites and structure properties such as wall thickness.

Introduction

Pressure vessels and piping made from fiber-reinforced plastics (FRP) have several attractive properties such as a high strength-to-mass ratio and high-corrosion resistance. The manufacturing of tubular composite structures occurs predominately by filament winding and related processes, which combine efficient fabrication with good quality relating to repeatability and strength properties. Thermoset polymers such as epoxies and polyesters are most widely used as matrix materials due to the ease of processing, good chemical and thermal stability, as well as cost competitiveness. Linerless vessel and pipe structures are particularly attractive since they offer significant mass and cost savings over their lined counterparts [1]. However, it is a well known that composite pipes and vessels without metallic and polymeric liners are subject to various types of leakage failures over a wide range loading conditions [2]. Leakage events usu-

ally occur well below pressures causing mechanical failure such as bursting. Leakage is induced by fractures in the polymeric matrix phase that initiate early during mechanical loading, thermal cycling and even during elevated temperature curing procedures. The leakage phenomenon in composite structures containing pressurized fluid was studied previously by other researchers, with particular focus on components for cryogenic service. For example, in recent studies [3-4] the conductance of leakage paths formed by transverse matrix cracking (TMC) and delamination was investigated, and an attempt was made to predict the leakage rate through damaged laminates. The underlying damage mechanisms that generally are considered to be responsible for leakage events, i.e. TMC and delamination, are rather well understood and have been researched extensively (see e.g. [5] for a review on associated failure models). In this context an idealized homogeneous configuration of a fiber-reinforced composite is usually assumed for the purpose of analysis and modeling. This generally implies a periodic distribution of the fiber reinforcement in the matrix phase on the micro and meso-scale (here, micro scale refers to a resolution level of micro features such as individual fibers, fiber agglomerations, voids and resin pockets, whereas meso-scale takes into account periodic cell structures in laminates with interlaced patterns). In reality, however, inhomogeneities in the composite microstructure [6] and meso-scale periodicity affect the mechanical response and evolution of damage to a great extent. This is often the case for filament-wound composites due to the deposition of distinct fiber bands, which generally causes fiber band undulations (see e.g. [7]) as well as zones either rich in resin or fiber content, and micro-void entrapment. It has been shown that undulations in composite laminates cause heterogeneous mechanical responses, see e.g. [8-9], which can be visualized using strain mapping techniques such as digital image correlation technique. As discussed in [8], characteristics of matrix damage initiation in such laminates have been the subject of earlier studies. However, the effects of inhomogeneities at the micro and meso-scale on matrix cracking and resulting leakage events have not been investigated extensively. Few studies considering the analyses of internal damage, including TMC, through X-ray computed microtomography (μ -CT) have been reported in the technical literature. Schilling et al. [10], for example, investigated damage in FRP using a commercial μ -CT apparatus. They showed that micro-damage features such as voids and matrix cracking can be resolved in small-scale samples, which dimensions are limited to the millimeter range.

The present paper describes findings from an experimental study which aim is to assess inhomogeneities of filament-wound composite tubes. This includes the mapping of (a) surface strains during mechanical loading, and (b) material and structural characteristics such as wall thickness. An attempt was made to establish a corre-

lation between locations of observed leakage damage and local deviations from global strains as well as average material and structure properties. For that purpose, thin-walled tubular specimens were produced and subjected to mechanical testing with internal pressurization. In addition to test data that was collected during the experiments through conventional means, e.g. information on loadings and pressurized fluid volume, digital images were recorded in-situ for mapping of surface strains and leakage initiation locations in post-processing operations. Following the experiments, specimens were further investigated employing μ -CT.

Mechanical Testing

Advantex® glass fiber roving (158B Type 30 by Owens Corning) with a linear mass of 735 g/km (671 yds/lb) and average filament diameter of 13.4 μ m was used to filament-wind tubular samples. The polymer matrix was a bisphenol-A epoxy system with a non-MDA polyamine hardener (EPON826 resin with EPICURE9551 by Hexion Specialty Chemicals). Manufacturing occurred using an industrial-type winding machine (WMS-4 axis by McClean-Anderson). Winding bands formed by eight glass fiber strands were wrapped simultaneously onto chrome-plated steel mandrels with a diameter of 38.1 mm (1.5 in). For certain specimens, colored glass fiber tracer threads were used to mark the sides of winding bands to facilitate a later identification of the winding band pattern. A numerical controlled tensioner applied a tensile force of 27 N (6 lb) to each fiber strand. The winding angle was 45°. The ensuing width of the winding band required four passes of the machine carriage to achieve full coverage of the mandrel. Consequently, fiber band undulations were present in the composite laminate. Only a two-layer laminate was produced, and hence the fiber architecture designation for the tubes used in this study was [\pm 45°]. Curing at elevated temperatures occurred according to recommendations by the resin manufacturer. Following curing, mandrels were extracted, and composite tubes were cut to length. Aluminum end connections were attached to the specimens by adhesive bonding. A photograph of a specimen is shown in Figure 1. The free gauge length of the exposed composite tubes was 90 mm (3.5 in).

Some tube samples were subjected to a resin burn-out procedure to measure the composite fiber volume fraction (FVF). Prior to burning off the resin, samples were machined to approximately 75% of their initial average wall thickness, which removed the resin layer on the tube outside surface that formed by the accumulation of excess resin during the winding procedure. An average FVF of 65% was thus determined for the predominately load-bearing fiber bed. An effective wall thickness of 0.58 mm was calculated based on the FVF and other manufacturing parameters (i.e. number of strands and their linear mass and material density, and number of

winding circuits to produce a two-layer laminate) [11]. The effective wall thickness neglects the thickness of the surface resin cover which is usually rather inconsistent; hence, the effective wall thickness is that of the aforesaid load-bearing fiber bed.

Mechanical testing of tubular specimens was conducted using a custom-built multi-axial testing apparatus. A computerized controller and data-acquisition system adjusted axial traction and internal pressurization to achieve an equi-biaxial hoop-to-axial stress state. The pressure medium was hydraulic oil, and a monotonic pressure loading rate of 2.35 kPa/s (0.34 psi/s) was applied. The hydraulic system was equipped with instrumentation to measure the amount of fluid supplied to the specimen. From this data, the fluid loss of the specimen and therefore the onset of specimen leakage could be determined [12]. Specimens were also equipped with bidirectional electrical resistance strain gauges to corroborate strain data obtained from digital imaging.

Digital Imaging

A digital image correlation system was employed to generate full-field strain measurements (Vic-3D by Correlated Solutions). Two CCD cameras (AVT Pike F421b) with 28-85 mm zoom lenses (Nikon) provided a resolution of 2048 x 2048 pixels. The cameras were positioned to have a distance of about 0.15 m (6 in) between lenses and specimen surface. The angle between their optical axes was 30° to 40°.

Regular white and black spray paint was used to create a unique speckle pattern on the surface of each specimen. The area thus marked defined the 'area of interest' which was subject to investigation. Figure 2 shows a specimen including pattern area after installation into the testing machine. On each specimen the area of interest was axially oriented covering a rectangular area with dimensions of 38.1 mm by 50.8 mm (1.5 in by 2.0 in). Strain gauges were located in opposite corners of the rectangular pattern area. The size of black speckles on the white background was ascertained to range from 30 μ m to 250 μ m (1181 μ in to 9843 μ in), which in the camera image corresponds to an apposite speckle size range between 1 and 7 pixels. A curved white reflector in conjunction with halogen lighting provided bright and uniform specimen illumination without glare. Black adhesive tape was used to suppress light reflections on remaining smooth specimen surfaces. Since the lighting was found to raise the specimen temperature, an ambient airstream was directed through a special enclosure onto the specimen, creating a steady-state specimen test temperature of 29°C (84°F).

During the test, images were recorded at a frequency of 2 Hz. Employing the DIC method in a post-processing operation, strains were computed using a cor-

relation subset of 17 x 17 pixels, which corresponded to image subsets showing three to five speckle dots. The step size for the subset offset was set to four pixels. These settings provided good correlation results, i.e. the average error and standard deviation for image series taken of specimens without applied loading were found to be less than 20 μ strain.

The emergence of oil droplets on the specimen surface rendered optical strain measurements through the DIC procedure impossible. Nevertheless, recording of images after the appearance of oil droplets permitted the determination of leakage initiation sites. Since specimens were subject to dimensional changes during testing, the exact leakage locations were determined using specific speckles as opposed to image pixel locations. As an example, a speckle pattern and superimposed leakage initiation sites (red dots) are shown in Figure 3 for a specimen identified as B002.

Computed Microtomography

An investigation of samples through computed microtomography was conducted employing a Skyscan 1076 x-ray scanner. 3D image reconstruction, analysis and visualization was accomplished using Skyscan software including NRECON, CT-An and CT-Vol. X-ray image acquisition took place at a source voltage and current of 49 kV and 100 μ A respectively. Filtering occurred with 0.5 mm aluminum. For every specimen three sets of cross-section slice images were taken in order to capture the complete volume associated with aforesaid area of interest. Each set consisted of 384 images with a 525 X 1000 pixel resolution. The image pixel size corresponded to a physical dimension of 34 μ m. The image brightness gradation was 16 bit. The three image sets were subsequently combined to a full representation of the area of interest.

Experimental Results and Discussion

Leakage and strain measurements:

As described above, the amount of fluid supplied to the specimen was measured by the test system. This data was corrected for fluid compressibility and expansion characteristics of the hydraulic system and the specimen. The latter was accomplished using additional strain gauge rosettes attached to the center of the specimen gauge length. Making these corrections the fluid transmission through the specimen wall was obtained. For example, the graph in Figure 4 shows the fluid leakage of specimen B002 with respect to the applied pressurization. At the start of the test, a steep rise of the curve can be observed. This behavior is caused by strong compressibility effects such as those associated with traces of air present in the hydraulic system. Then the curve reaches a plateau indicating that no fluid was leaking.

Finally, a steep rise in the curve signifies the occurrence of specimen leakage. The leakage failure point shown in Figure 4 corresponds to an arbitrarily set fluid loss, i.e. 200 mm³ (0.012 in³). Leakage failure thus defined occurred for this particular specimen at an internal pressurization of 4.8 MPa (700 psi). It shall be mentioned that fluid droplets were usually observed to emerge at pressures considerably lower than the values obtained from the leakage analysis. For the current specimen, the first sign of fluid leakage was found at 3.8 MPa (550 psi) through careful visual inspection of the images contained in the test database. The DIC procedure for optical strain measurement was aborted at 4.7 MPa (680 psi). It is noteworthy that the leakage behavior observed with present thin-walled specimens was in its appearance indistinguishable from leakage seen on specimens with greater wall thickness and same diameter; that is, the occurrence of small droplets on the specimen surface is considered a typical 'weepage' damage mode.

Strain data obtained from gauges corresponded well with surface averaged values computed by the DIC method. This can be observed in Figure 5 where example strain data for specimen B002 is depicted. Hence, present experiments confirmed that DIC is a reliable contactless method for measuring strains on composite specimens. Notably, measured strains were nonlinear, with circumferential strains being about 30% higher with respect to hoop strains. All specimens tested in this study exhibited this behavior. Albeit not important for the present investigation, this behavior is somewhat remarkable. Based on the specimens' [$\pm 45^\circ$] fiber architecture and the applied equi-biaxial stress loading condition, an equally equi-biaxial material response was expected, resulting in equal strains in hoop and axial directions. The observed behavior cannot be explained conclusively at this point, yet it may be speculated that the tubular structure of the samples is responsible for the deviation from truly orthotropic characteristics (for example, residual stresses may have been present in the structure, which are more likely to build-up in the hoop direction during manufacturing).

The experiments showed that the employed digital imaging techniques are practically equivalent to conventional techniques for the global quantification of the mechanical response to applied loadings. However, for the assessment of local effects, which is the focus of the present study, it is hardly possible to use the conventional techniques. For instance, the assessment of leakage through digital imaging is not only much more sensitive than the method based on fluid volume loss, but also provides the precise locations of leakage initiation.

Surface strain mapping:

Strain maps obtained through the DIC method can easily be combined with image data for leakage initiation

sites. Shown in Figure 6 is the evolution of axial surface strains with increasing applied loading. Note that maps for hoop strain were not included here since they are quantitative very similar to the depicted axial strain data. In Figure 6 leakage initiation sites are depicted as white dots. The top and bottom strain maps in this figure correspond to zero loading and loading just prior to the emergence of leakage respectively. It can be observed that strains exhibited, to some extent, a periodic pattern, i.e. with increased loading, zones/bands of high and low strains evolved that were aligned with the $\pm 45^\circ$ fiber orientation. Inspection of Figure 6 shows that no conclusive correlation exists between sites of observed leakage initiation and zones of high or low strain. Moreover, leakage spots did not form any consistent pattern matching the bands of high or low strain.

Since some specimens were manufactured with aforementioned tracer threads that marked individual winding bands, strain inhomogeneities could also be analyzed taking the winding band locations into consideration. In Figure 7 an axial strain map is presented onto which the winding band pattern was superimposed (for specimen B003). Parallel blue and green lines that are in close proximity to each other indicate a slight winding band overlap that was adjusted to achieve a uniform distribution of fiber reinforcement without gaps between winding bands. Figure 7 shows that despite a general alignment between the strain pattern and the winding band tracers, no distinct correspondence between zones of elevated strains and winding band location is apparent. It is interesting to note that locations of observed leakage initiation frequently coincide with the tracer threads, i.e. the sides/edges of winding bands. This deduction is supported by imaging from other specimens, for example, specimen B004 shown in Figure 8. Hence, it was conjectured that leakage has a higher probability to occur at winding band edges. However, no general conclusion can be drawn here based on the limited amount of data.

Computed Microtomography:

In contrast to the investigation reported in [10] the current study did not attempt to resolve individual microdamage features such as matrix cracking through computed microtomography. (Even though the scanning equipment would have been capable to provide the required resolution.) Achieving the resolution required for such undertaking would generate excessively large datasets for the relatively large regions of interest considered in this study. Rather, the goal of current analyses was to map areal features such as wall thickness irregularities. Figure 9 shows the X-ray shadow projection for specimen B004. Note that Figure 8 (optical image) and Figure 9 (X-ray image) correspond to each other with respect to the north-south orientation; however, Figure 9 does not fully match the area of interest shown in Figure 8 since a slightly different circumferential image ori-

entation was adjusted during X-ray imaging. A challenge during the current investigation was accurate image registration between optical and X-ray images. At the time of the preparation of this paper, different types of image markers for image registration (e.g. metal targets) were under consideration that provide good visibility in the optical as well as the X-ray domain. However, appropriate image processing techniques for the comparison of datasets from optical and X-ray analyses were not available yet, which were subject to future work.

A reconstructed (three-dimensional) volumetric model of a specimen surface topography is shown in Figure 10 (for specimen B004). In this model the resin surface cover, which gives a specimen its glassy, smooth surface (see Figure 1), was rendered invisible based on the poor X-ray attenuation of the pure resin material. In addition, areas containing strain gauges were excluded because metallic components associated with the gauges produced artifacts that considerably degraded local image quality. In Figure 10 image pixels correspond to a physical dimension of $34\ \mu\text{m}$, which is considerably larger than the average filament diameter. Consequently, individual filaments were not resolved. The model therefore depicts a blended fiber-resin structure that is equivalent to aforementioned load-bearing fiber bed. The figure clearly shows that the associated model surface is noticeably uneven, and zones/bands with different wall thicknesses exist. Due to aforementioned unresolved challenges regarding image registration, an accurate correlation between leakage initiation sites, strain patterns and model surface topography was not possible. Yet, it can be observed that bands of elevated surface strain in Figure 8 (green and yellow hues) match the orientation of the valleys and ridges visible of the volumetric model in Figure 10. Hence, one may conjecture that elevated surface strains are caused by thickness variations in the composite fiber bed and possibly associated microdamage features (matrix cracking).

For the three sets of cross-section images taken from specimen B004 the wall thickness was approximated using the trabecular thickness (Tb.Th) method in conjunction with a sphere model. Herein the transition zone between image sets was neglected to avoid including artificial thickness data from the image subset reconstruction and merging process. Figure 11 shows a graph comparing the effective wall thickness (0.58 mm) and wall thickness data determined through μ -CT. From these data it becomes evident that the effective wall thickness is less than the average wall thickness estimated from the Tb.Th method (0.70 mm). It was inferred that this deviation is caused by distributed void space within the sample and resin-rich fiber composite on the sample surface, given that they influence measurements from the Tb.Th method but are neglected in the case of the effective wall thickness.

Conclusions

This paper presents a study dealing with filament-wound fiber-reinforced polymer composite tubes that were subjected to mechanical loading including internal pressurization. The investigation included the assessment of surface strains and leakage initiation sites through digital imaging. Furthermore, computed microtomography was employed to visualize the topography of the load-bearing fiber composite bed, i.e. the composite structure devoid of accumulated resin forming a surface cover. The following conclusions and recommendation resulted from the investigation.

- Digital imaging produced precise surface maps showing the sites of leakage initiation for pressurized composite tubes. Leakage assessment using digital imaging was found to be significantly more sensitive than measurements based on fluid volume loss.
- Digital image correlation technique using white-light and monochromatic speckle patterns was found well suited to produce detailed surface strain maps for composite specimens. Surface averaged strain data agreed well with local strain values obtained from conventional strain gauge measurements.
- For elevated loading conditions approaching specimen leakage failure, surface strain patterns were found to be highly inhomogeneous, featuring zones/bands with considerably different strain magnitudes. A direct correlation between surface strain pattern and leakage spots could not be ascertained. It was however observed that leakage initiation occurred more frequently at the edges of the fiber bands deposited during filament winding.
- Analysis of reconstructed volumetric models from computed microtomography images showed that the composite fiber bed featured considerable thickness variations that manifested themselves through the existence of ridges and valleys. These features matched in their orientation the strain patterns that were visualized through digital imaging.
- Obtaining direct correlations of surface strain patterns and leakage initiation sites from digital imaging with volumetric models from μ -CT seems feasible. But, to achieve this, a reliable technique for image registration is required, which was not available during the preparation of the present study. Future work should therefore include the development of markers that can precisely be detected in optical as well as μ -CT images.
- In this study, areas of interest sampled through μ -CT were relatively large, and therefore the scanning resolution was limited to avoid prohibitively large datasets. As a consequence, micro-scale features (cracks, micro-voids) were not resolvable. To enable

analyses on the micro-scale in combination with the present characterization of meso/macro-scale features, additional scanning of specific sample subregions (e.g. leakage initiation zones) at higher resolutions would be required. Such a multiscale approach would again require a method for precise image registration.

- It was shown that the computation of wall thickness data through μ -CT is possible using e.g. the trabecular thickness method in conjunction with a sphere model. In the current study, the average wall thickness calculated in this manner was found to be greater than the effective specimen wall thickness, which was computed from the specimen fiber volume fraction and manufacturing parameters. The reasons considered for this discrepancy were distributed void space within the sample and resin-rich fiber composite on the sample surface, which affect trabecular thickness measurements but not the effective wall thickness.

Acknowledgments:

The authors would like to acknowledge the contributions by Canadian Foundation for Innovation and the Natural Sciences and Engineering Research Council of Canada.

Authors:

Mohammad Abdelghani, Student,
Kari Arnston, Student,
Pierre Mertiny, Assistant Professor
Department of Mechanical Engineering
University of Alberta, Edmonton, Alberta, Canada

Renke Scheuer, Student
Institute of Materials Science
Leibniz Universität Hannover, Hannover, Germany

YuChin Wu, Student
Martin Doschak, Assistant Professor
Faculty of Pharmacy & Pharmaceutical Science
University of Alberta, Edmonton, Alberta, Canada

References:

1. K. Ryan, et al. 47th AIAA/ASME/ASCE/AHS/ASC Structures, Structural Dynamics, and Materials Conference, 10, 7236 (2006).
2. S.J. Roberts, et al. J. Compos. Mater., 37, (17), 1509 (2003).
3. P. Peddiraju, et al. J. Compos. Mater., 41, (1), 41 (2007).
4. H. Kumazawa and J. Whitcomb, J. Compos. Mater., 42, (16), 1619 (2008).
5. M.R. Garnich and V.M.K. Akula, Appl. Mech. Rev., 62, (1), 010801 (2009).

6. F. Ellyin and C. Grufman, *Compos. Sci. Technol.*, 67, (3-4), 766 (2007).
 7. Y. Zhang, Z. Xia and F. Ellyin, *Int. J. Solids Struct.*, 45, (20), 5322 (2008).
 8. D. Ivanov, et al., *Opt. Lasers Eng.*, 47, (3-4), 360 (2009).
 9. N.O. Cabrera, et al., *Appl. Compos. Mater.*, 15, (1), 27 (2008).

10. P. Mertiny and A. Gold, *Polym. Test.*, 26, (2), 172 (2007).
 11. P. Mertiny and F. Ellyin, *Compos. A*, 33, (12), 1615 (2002).
 12. P.J. Schilling, et al., *Compos. Sci. Technol.*, 65, (14), 2071 (2005).

Figures:

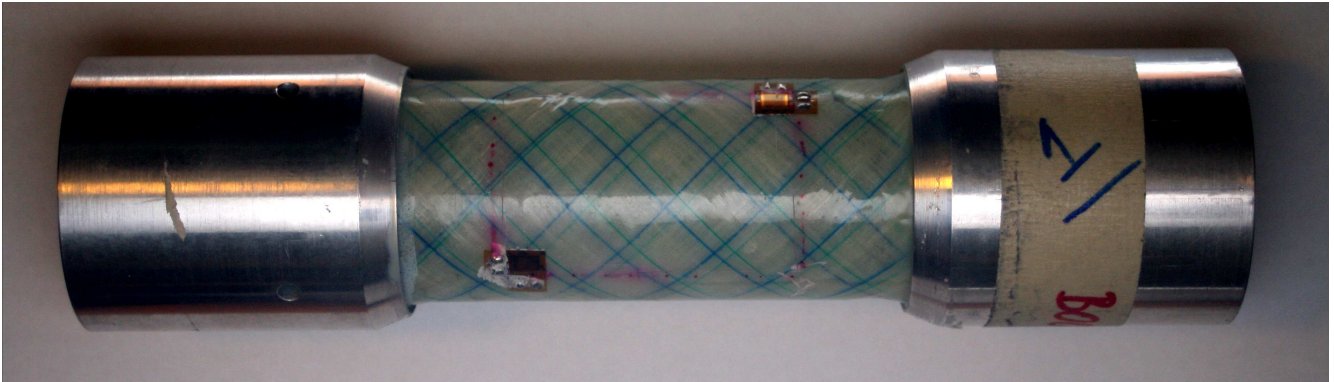


Figure 1: Tubular specimen (Spec.-ID: B004).



Figure 2: Specimen in testing apparatus.

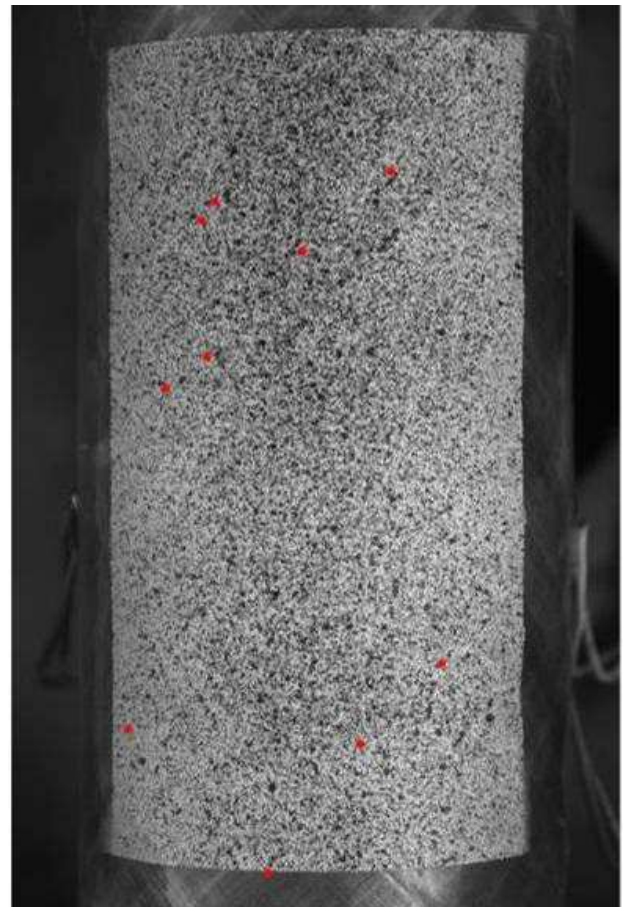


Figure 3: Markings (red dots) indicating leakage sites on specimen surface (Spec.-ID: B002).

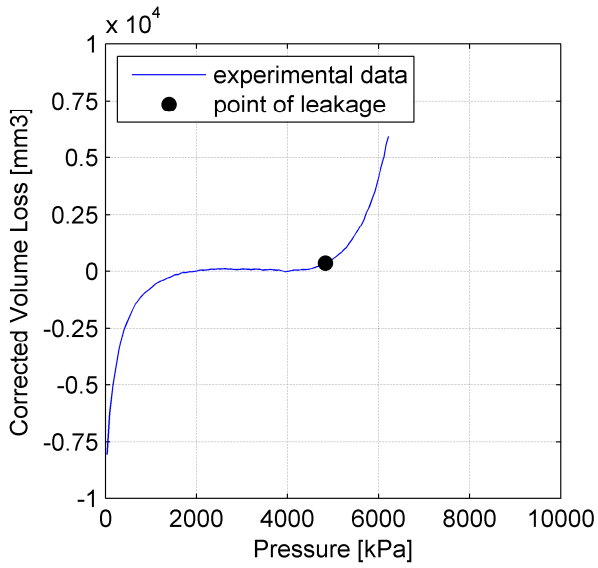


Figure 4: Specimen leakage curve (Spec.-ID: B002).

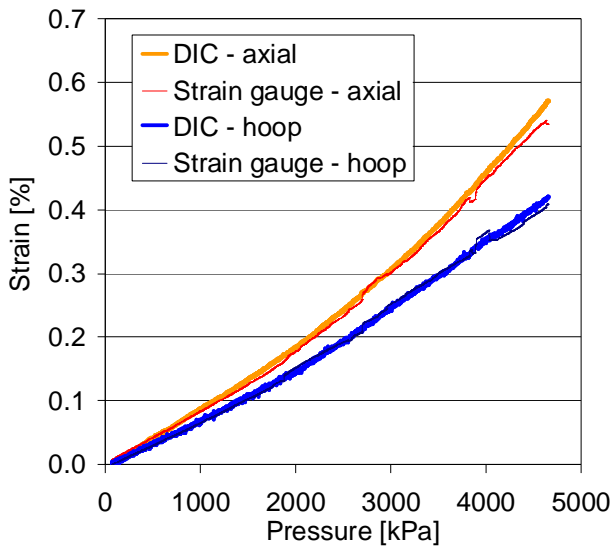


Figure 5: Strain data from gauges and image analysis (Spec.-ID: B002).

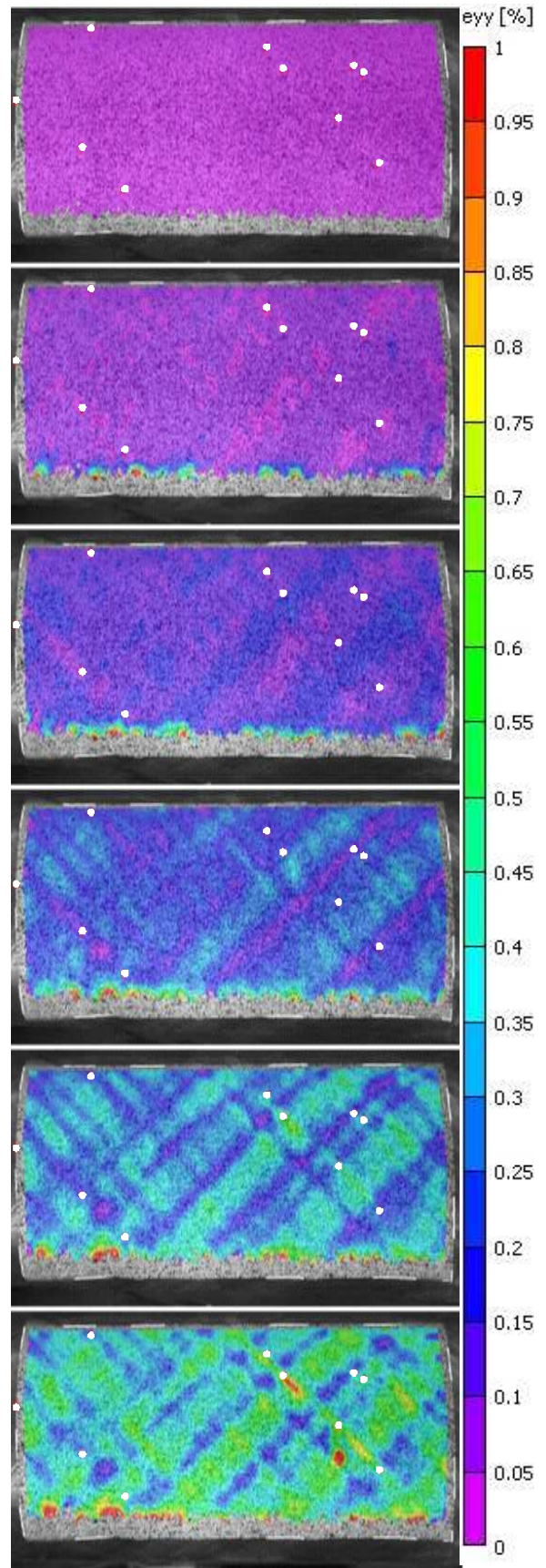


Figure 6: Axial strain maps with superimposed leakage sites (white dots) (Spec.-ID: B002).

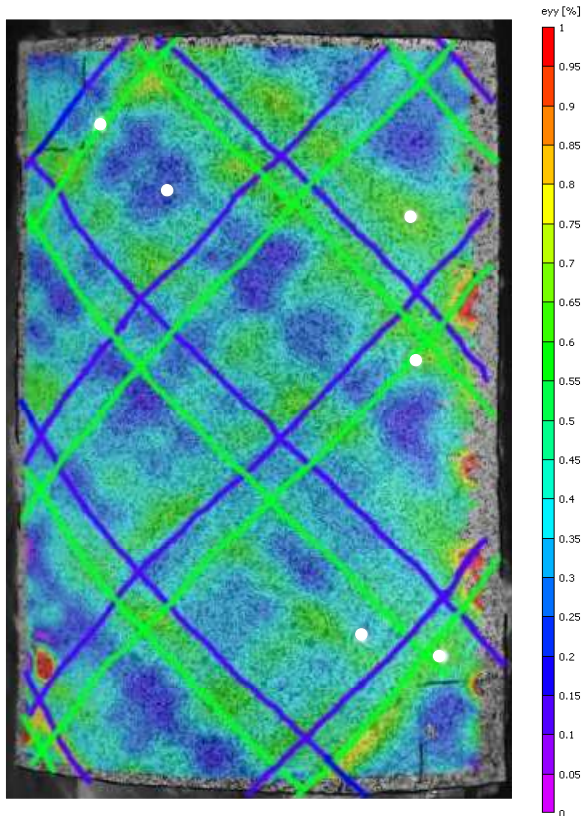


Figure 7: Axial strain maps with superimposed winding band pattern (blue and green lines) and leakage sites (white dots) (Spec.-ID: B003).

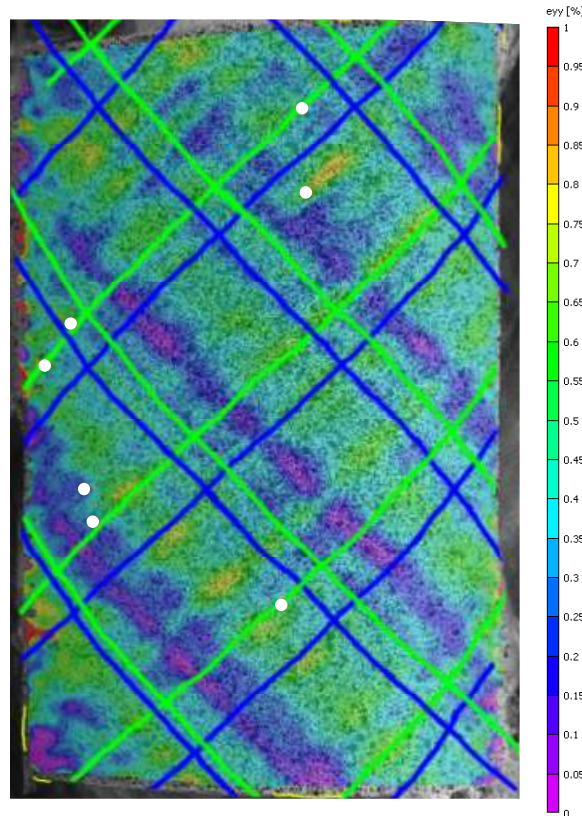


Figure 8: Axial strain maps with superimposed winding band pattern (blue and green lines) and leakage sites (white dots) (Spec.-ID: B004).

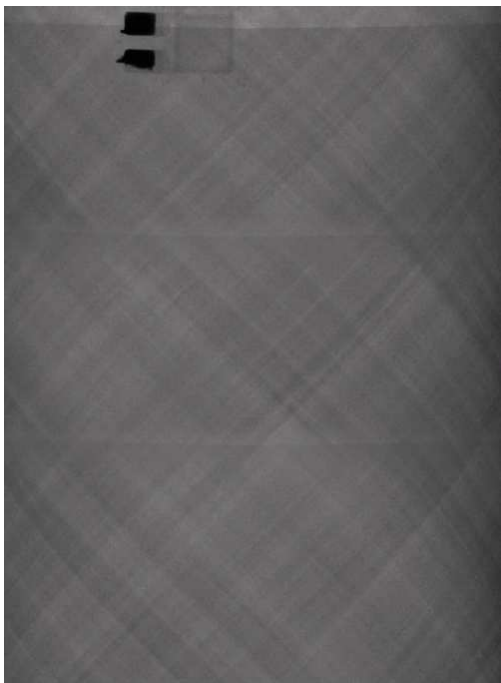


Figure 9: μ -CT shadow projection of specimen B004.

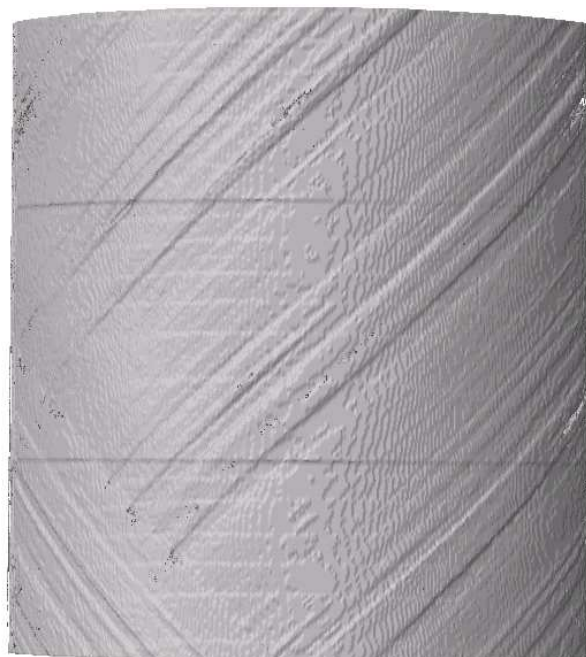


Figure 10: Three-dimensional volumetric model of specimen surface topography excluding resin surface cover (Spec.-ID: B004).

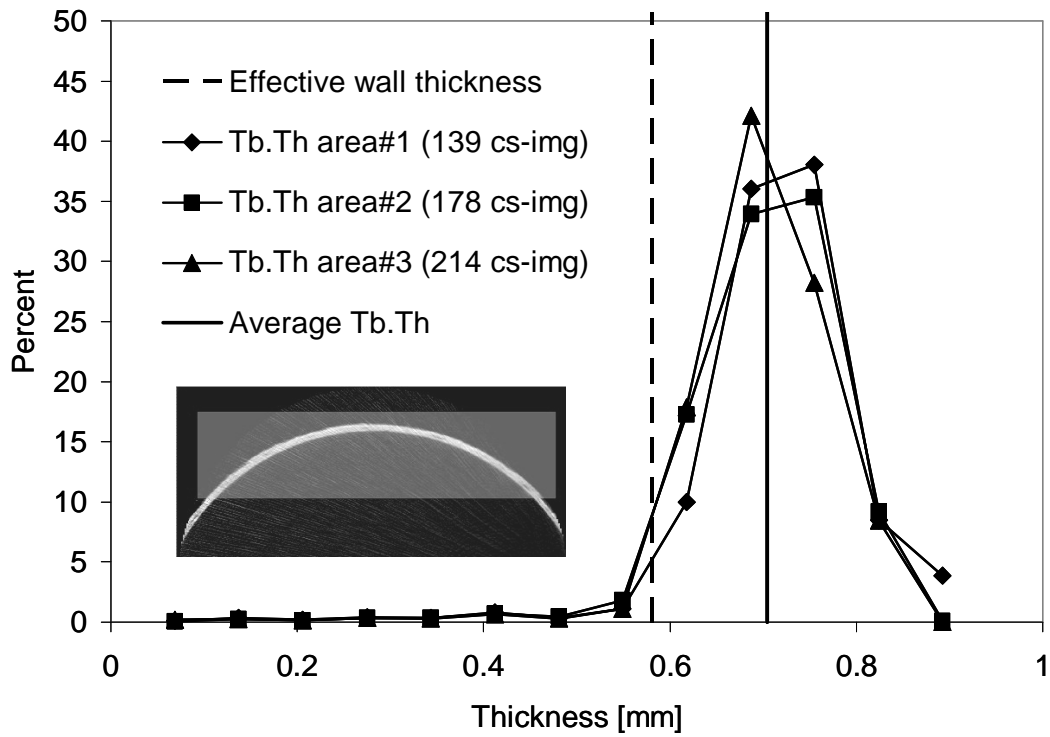


Figure 11: Effective wall and distributions and average value of trabecular thickness (Tb.Th) for specimen B004. Number of cross-section images from image set #1 to #3 is indicated as n cs-img. Insert showing measurement region (grey box) in sample cross-section image.